Computation of spherical harmonic representations of source directivity based on the finite-distance signature

Computation of Spherical Harmonic Representations of Source Directivity Based on the Finite-Distance Signature

Jens Ahrens and Stefan Bilbao

***Abstract*—The measurement of directivity for sound sources that are not electroacoustic transducers is fundamentally limited because the source cannot be driven with arbitrary signals. A consequence is that directivity can only be measured at a sparse set of frequencies—for example, at the stable partial oscillations of a steady tone played by a musical instrument or from the human voice. This limitation prevents the data from being used in certain applications such as time-domain room acoustic simulations where the directivity needs to be available at all frequencies in the frequency range of interest. We demonstrate in this article that imposing the signature of the directivity that is obtained at a given distance on a spherical wave allows for all interpolation that is required for obtaining a complete spherical harmonic representation of the source's directivity, i.e., a representation that is viable at any frequency, in any direction, and at any distance. Our approach is inspired by the far-field signature of exterior sound fields. It is not capable of incorporating the phase of the directivity directly. We argue based on directivity measurement data of musical instruments that the phase of such measurement data is too unreliable or too ambiguous to be useful. We incorporate numerically-derived directivity into the example application of finite difference time domain simulation of the acoustic field, which has not been possible previously.**

***Index Terms*—Sound radiation, spherical harmonics**

I. Introduction

THE measurement and modelling of sound source directivity has seen increased interest in recent years. The main application areas are the analysis of the directivity of, for example, musical instruments in order to understand the impact on the listening experience [1], how the directivity interacts with room acoustics [2], [3], how noise from machinery propagates in a given environment [4], or virtual reality [5]. Source directivity and even more so dynamic source directivity have been shown to increase plausibility as well as other favorable psychoacoustic attributes of auralizations [6].

Simple models for directivity include [6], [7], [8] in which the directivity is represented by radiated rays or beams. Spherical harmonics (SH) have been shown to be a powerful representation of sound source directivity [9], [10], going back to early work by Weinreich [11]. We will focus on wave-based room acoustical simulations such as [12] as an application scenario in the present article because it is this case that both places the most stringent requirements on the modelling of the sound source directivity and allows for the most accurate simulation of the acoustic field. Specifically, the directivity needs to be available with respect to magnitude and phase at any arbitrary frequency in a continuous-space representation such as an SH expansion.

The incorporation of source directivity into geometrical acoustics has seen some investigation. Spatial resolution of source directivity was studied in [3]; a significant impact of the maximum SH order of the directivity on room acoustical metrics was found with saturation occurring at an SH order of around 10. It was found in [13] that directivities of order higher than 4 were not perceptually significant in a binaural auralization of an image source-based room simulation.

A major challenge is the measurement of directivities of sources that are not electroacoustical transducers. This is mainly because it is not possible with most sources to drive them in a reproducible manner with a known input signal as in the case of, e.g., musical instruments or machinery. Most of the available data comprise polar plots or similar of the radiated magnitude or power for a given representative signal. Many times, no information on the phase is available. Examples are [14] (human voice), [1], [15] (musical instruments), [16], [17] (vehicles), [18] (wind turbines), and [19] (loudspeakers). Data on violins that were excited in an automized manner are presented in [20].

The musical instrument directivities presented in [21] were measured using a spherical array of 32 microphones surrounding a musician playing single tones and scales at different dynamic levels. The directivity was defined as the magnitude and phase that were deduced from each of the microphone signals at the corresponding frequencies of stable partial oscillations.

Some attempts have been made to compute spherical harmonics based representations for directivities of non-electroacoustic sound sources [22], [23]. They are limited to individual selected frequency bins of the DFT spectrum. We therefore consider the resulting SH representations *incomplete* as they do not represent the directivity at all frequencies in the frequency range of interest.

Conceptually, the directivity represents a whole set of information, including the location of a radiating surface, time-frequency information as well as the propagation of the radiated sound field. The limitations of the measurement procedures do not allow for all this information to be represented

J. Ahrens is with the Division of Applied Acoustics at Chalmers University of Technology, 412 96 Gothenburg, Sweden; e-mail: jens.ahrens@chalmers.se

S. Bilbao is with the Acoustics and Audio Group, Reid School of Music, University of Edinburgh, Edinburgh, United Kingdom; e-mail: s.bilbao@ed.ac.uk

Manuscript received XXX XX, XXX; revised XXX XX, XXX.

in the data. In most cases, the phase data are either not available at all (as explained above) or unreliable as we will illustrate in Sec. V-C.

We therefore applied an approach in [24] that consists in imposing source position and curvature of the wave front as well as the angle-dependent magnitude directivity onto a spherical wave. The present article contributes further analysis of the method in terms of the distance dependency of the resulting directivity representation as well as of the effects of order truncation.

A similar approach had already been employed in the modeling of the directivity of moving sources in [25] and with the boundary element method in [5], but its properties were not investigated further.

Source directivity and the proposed approximation are presented in Sec. II and III. The accuracy of the proposed approximation is discussed in Sec. IV. Numerical results based on publicly available directivity data are presented in Sec. V. We concentrate here on musical instruments as these are amongst the most challenging types of sound source in terms of the sparsity of the measured directivity. We have presented related work on the examples of a sparsely measured directivity of a singing voice as well as of data in the Common Loudspeaker Format in [26].

II. Source Directivity

The term *directivity* with regard to acoustic sources has been defined in various ways in the literature [27], [19], [28], [29, p. 204]. Here, we define directivity as the spatio-temporal transfer function of a sound source under free-field conditions, evaluated at arbitrary spatial locations. This is the most general definition, from which the others above can be derived. We will assume that the directivity is evaluated on a spherical surface centered around the source and omit the assumed time dependency of $\mathrm{e}^{-\mathrm{i}\omega t}$ (following the sign convention used in [29]).

A source directivity $W(r, \boldsymbol{\gamma}, \omega)$ is dependent on an angular frequency ω, in rad/sec, a radial distance r in m from the nominal source center, and a unit-length 3-vector $\boldsymbol{\gamma} = [\cos\alpha \sin\beta,\ \sin\alpha \sin\beta,\ \cos\beta]^T$ defined in terms of azimuth angle α and colatitude β. The directivity is defined as

$$W(r, \boldsymbol{\gamma}, \omega) = \sum_{l=0}^{\infty} \sum_{m=-l}^{l} \underbrace{\breve{W}_{l,m}(\omega) h_l^{(1)}\left(\omega \frac{r}{c}\right)}_{=\mathring{W}_{l,m}(r,\omega)} Y_{l,m}(\boldsymbol{\gamma}) \,, \quad (1)$$

and represents the radiated acoustic field exterior to a sphere that is just large enough to completely enclose the sound source [29, p. 206]. We will refer to (1) as the *conventional representation* of directivity in the remainder of this article. $h_l^{(1)}(\cdot)$ is the lth order spherical Hankel function of first kind, and $Y_{l,m}(\boldsymbol{\gamma})$, defined for integer $l \geq 0$ and $-l \leq m \leq l$, are the SH basis functions, which we are assuming to be real and orthonormal over the unit sphere. $\breve{W}_{l,m}(\omega)$ are coefficients that contain all information about the source directivity. Our choice of time dependency makes $h_l^{(1)}(\cdot)$ represent an outgoing wave.

The coefficients $\breve{W}_{l,m}(\omega)$ follow from

$$\breve{W}_{l,m}(\omega) = \frac{1}{h_l^{(1)}\left(\omega \frac{R}{c}\right)} \iint_{S^2} W(R, \boldsymbol{\gamma}, \omega) Y_{l,m}(\boldsymbol{\gamma}) \mathrm{d}\Omega \,, \quad (2)$$

where $W(R, \boldsymbol{\gamma}, \omega)$ is a directivity known on a spherical surface with radius R that encloses the source, S^2 represents the unit sphere, and Ω is an infinitesimal surface element on S^2. Alternatively, a least-squares fit of the coefficients $\breve{W}_{l,m}(\omega)$ or $\mathring{W}_{l,m}(r, \omega)$ to the spatially discrete measurement data points can be performed based on (1) as demonstrated below. In either case, only the coefficients up to a given order $l = L$ that depends on the number of measurement points can be obtained.

Consider the case of N measurement locations $\mathbf{r}_q = R\boldsymbol{\gamma}_q$, for angle vectors $\boldsymbol{\gamma}_q$, $q = 1, \ldots, N$. The associated measured directivities W_q can be arranged as a column N-vector $\mathbf{W} = [W_1, \ldots, W_N]^T$, whereby $(\cdot)^T$ denotes matrix transpose. Eq. (1), when truncated to order $l \leq L$ may be written in vector-matrix form as [30], [31], [12]

$$\mathbf{W} = \mathbf{Y} \mathring{\mathbf{W}} \,, \quad (3)$$

where here

$$\mathbf{Y} = \begin{bmatrix} Y_{0,0}(\boldsymbol{\gamma}_1) & Y_{1,-1}(\boldsymbol{\gamma}_1) & \ldots & Y_{L,L}(\boldsymbol{\gamma}_1) \\ Y_{0,0}(\boldsymbol{\gamma}_2) & \ddots & \ddots & Y_{L,L}(\boldsymbol{\gamma}_2) \\ \vdots & \ddots & \ddots & \vdots \\ Y_{0,0}(\boldsymbol{\gamma}_N) & Y_{1,-1}(\boldsymbol{\gamma}_N) & \ldots & Y_{L,L}(\boldsymbol{\gamma}_N) \end{bmatrix} \quad (4)$$

and

$$\mathring{\mathbf{W}} = \left[\mathring{W}_{0,0}(R, \omega),\ \mathring{W}_{1,-1}(R, \omega),\ \ldots,\ \mathring{W}_{L,L}(R, \omega)\right]^T \,. \quad (5)$$

If $N \geq (L+1)^2$, Eq. (3) can be solved in the least-squares sense by

$$\mathring{\mathbf{W}} = \mathbf{Y}^{\dagger} \mathbf{W} \,, \quad (6)$$

whereby $\mathbf{Y}^{\dagger}$ denotes the Moore-Penrose pseudo inverse [32]. The solution may be complemented by a regularization term, such as that due to Tikhonov [32, Eq. (6.10)], [30].

III. An Approximation of Source Directivity

Evaluating the directivity in the limit of $r \to \infty$ leads to the large-argument approximation of the spherical Hankel function given by (18) in App. B, and (1) simplifies to [29, p. 204]

$$W_{\infty}(r, \boldsymbol{\gamma}, \omega) = \frac{\mathrm{e}^{\mathrm{i}\omega \frac{r}{c}}}{r} \frac{c}{\mathrm{i}\omega} \sum_{l=0}^{\infty} \sum_{m=-l}^{l} (-\mathrm{i})^l \breve{W}_{l,m}(\omega) Y_{l,m}(\boldsymbol{\gamma}) \,. \quad (7)$$

$W_{\infty}(r, \boldsymbol{\gamma}, \omega)$ is referred to as the *far-field signature* of the directivity [33, p. 81]. Eq. (7) indicates that at a sufficient distance, a source of finite spatial extent radiates spherical wave fronts ($e^{\mathrm{i}\omega \frac{r}{c}}/r$), the complex amplitudes of which depend on the angle and are represented by the coefficients $\breve{W}_{l,m}(\omega)$. In other words, the angular dependence of the directivity is imposed onto a spherical wave. How far this sufficient distance has to be depends on the spatial extent of the source and its distance from the coordinate origin (which coincides with the nominal location of the source). The observation distance has

to be much larger than the largest dimension of the source. If the source is of small spatial extent and located at the origin of the coordinate system, the discrepancy will be very small. This assumption holds for most sound sources for which detailed directivity data are available, such as [21]. Note that classical polar diagrams display the magnitude of the far-field signature $W_\infty(r, \boldsymbol{\gamma}, \omega)$.

Inspired by (7), we follow the proposition from [25] to impose the nominal source location as well as a model of the propagation (particularly the radial dependency) on the measured data. As we will highlight in Sec. V-C, the phase data can generally not be measured reliably and are often too sparse to permit interpolation [26]. We therefore extract only the magnitude of the directivity from the measurement data and impose it onto a spherical wave that originates from the coordinate origin [5]. We use the symbol $W'(r, \boldsymbol{\gamma}, \omega)$ in the remainder of this paper to represent this new modeled directivity. More precisely, $W'(R, \boldsymbol{\gamma}, \omega)$, over the spherical measurement surface of radius R is given by [24]

$$W'(R, \boldsymbol{\gamma}, \omega) = |W(R, \boldsymbol{\gamma}, \omega)| \, \mathrm{e}^{\mathrm{i}\omega \frac{R}{c}} \mathrm{e}^{\mathrm{i}\phi(\boldsymbol{\gamma}, \omega)} \,. \tag{8}$$

We refer to $|W(R, \boldsymbol{\gamma}, \omega)|$ as the *finite-distance signature* of the directivity. Note that it comprises the distance attenuation from the source to the spherical measurement surface. The factor $\mathrm{e}^{\mathrm{i}\omega \frac{R}{c}}$ in (8) represents a constant pure delay, which maintains causality. An optional phase factor $\mathrm{e}^{\mathrm{i}\phi(\boldsymbol{\gamma}, \omega)}$ may be fitted to the observed magnitude spectra to design the time-domain structure of the signals. Obvious options are minimum phase or linear phase [34]. Also, augmentation of the data through recovery of the algebraic sign of lobes in the directivity based on the magnitude as proposed in [35] or using [36] may be applied.

We express $W'(R, \boldsymbol{\gamma}, \omega)$ in (8) in terms of SH (cf. (1)) as

$$W'(R, \boldsymbol{\gamma}, \omega) = \sum_{l=0}^{\infty} \sum_{m=-l}^{l} \mathring{W}'_{l,m}(R, \omega) Y_{l,m}(\boldsymbol{\gamma}) \,. \tag{9}$$

Note that the value of the proposed representation does not lie in the approximation of a given directivity. As demonstrated in [24], [26] and in Sec. V, the value lies rather in the fact that this representation enables the computation of complete SH representations even if the available data are sparse with respect to the angle and/or the frequency. As we will elaborate further in Sec. V, such computations require ignoring the phase either way (if it is available at all).

Eq. (9) may be solved for $\mathring{W}'_{l,m}(R, \omega)$ either using (2) (without dividing by $h_l^{(1)}(\cdot)$) or performing a least-squares fit according to (6). As before, this can be achieved only up to a certain order $l = L$ in practice.

Using [29, Eq. (6.94)], the complete SH based representation of $W'(r, \boldsymbol{\gamma}, \omega)$ is finally given by

$$W'(r, \boldsymbol{\gamma}, \omega) = \sum_{l=0}^{L} \sum_{m=-l}^{l} \mathring{W}'_{l,m}(R, \omega) \frac{h_l^{(1)}\left(\omega \frac{r}{c}\right)}{h_l^{(1)}\left(\omega \frac{R}{c}\right)} Y_{l,m}(\boldsymbol{\gamma}) \,. \tag{10}$$

Note that the combination of (8) and (10) forces the curvature of the wavefronts of the directivity to be spherical. This is because the phase factor $\mathrm{e}^{\mathrm{i}\phi(\boldsymbol{\gamma}, \omega)}$ in (8) will usually imply only very small timing differences between different directions at a given frequency compared to the timing differences that a non-spherical wave front curvature would cause at distance R. We refer to $W'(r, \boldsymbol{\gamma}, \omega)$ as *proposed representation* of directivity in the remainder.

IV. Accuracy of the Proposed Representation

The evaluation of the accuracy of the proposed representation is complex and hinges on the particulars of the sound source under consideration. We will use the two simple directivities of a displaced monopole and of a set of four displaced monopoles (which emulates a distributed source) as test cases.

A. Effects of Order Truncation

The coefficients $\breve{W}_{l,m}(\omega)$ and $\mathring{W}'_{l,m}(R, \omega)$ in (1) and (10), respectively, can only be computed up to a maximum order $l = L$ in practice. This constitutes a spatial bandwidth limitation which makes the bandlimited representation exhibit a slower spatial variation. A secondary effect is a modification of the time-frequency spectrum, which is linked to the order L via the Hankel function $h_l^{(1)}(\cdot)$. We discuss this aspect in the present section.

Usually, sound source directivities are measured with spherical or circular microphone arrays. A method for measuring directivities with distributed arrays under non-free-field conditions is presented in [37]. It is very likely when measuring the directivity of real-world sources that some parts of the radiating structure cannot be placed in the center of the setup.

We assume in the following the simplest possible source: a monopole source that is located at $\mathbf{r}_s = (0.3, 0, 0)$ m whose directivity $\mathrm{e}^{\mathrm{i}\omega \frac{|\mathbf{r}-\mathbf{r}_\mathrm{s}|}{c}} / |\mathbf{r} - \mathbf{r}_\mathrm{s}|$ is known at 1800 equiangularly spaced positions on a spherical surface centered at the coordinate origin with a radius of $R = 1$ m. We use these simulated measurement data to extract a conventional SH representation (1) of the directivity of order $L = 6$ by means of an unregularized least-squares fit according to (6)[1].

Fig. 1(a) illustrates the magnitude of this 6th-order directivity at two different frequencies using balloon plots. Note that all balloon plots in this article present the data on a linear scale. The original directivity is represented well at the depicted low frequency (higher row). At the high frequency, the order-limited conventional representation departs substantially from the original directivity (lower row). This departure occurs together with a high-frequency roll-off, which is a consequence of the properties of order-limited translated SH expansions [38], [39]. The roll-off is clearly visible in the middle plot of Fig. 1(b) and can cause an attenuation in the order of 20 dB. The roll-off occurs also for distributed sound sources like that shown in Fig. 2 (middle plot). Note that this roll-off does not occur for compact sources located in the origin of the coordinate system.

[1]Note that the results are identical when using the analytical expressions of the SH representation of the displaced monopole (that are obtained via (2)) instead of the least-squares fit due to the orthogonality of the SH and the linear independence of the spherical Hankel functions in (1).

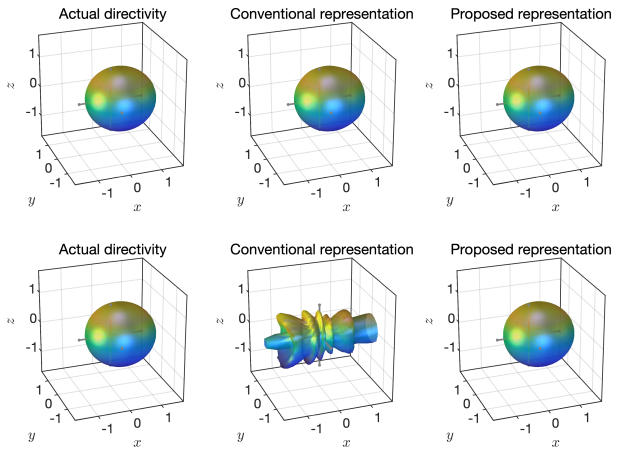

(a) Balloon plots of the conventional directivity representation (1) (middle column) vs. the proposed representation (10) (right column). Top row: $f = 600$ Hz. Bottom row: $f = 1500$ Hz.

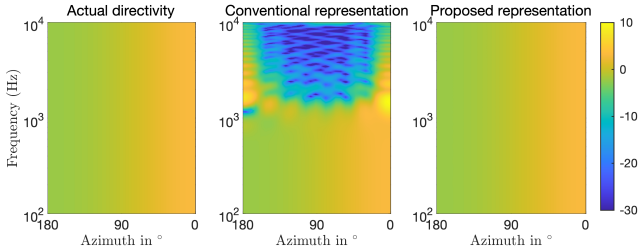

(b) Magnitude in dB of the directivity in the horizontal plane

Fig. 1. Magnitude of the directivity of a 6th-order approximation of a monopole displaced by 0.3 m from the coordinate origin in positive x-direction evaluated at 1 m distance in the horizontal plane

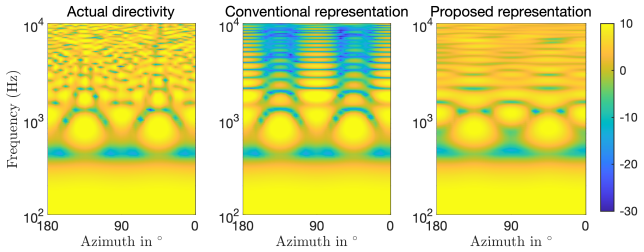

Fig. 2. Magnitude in dB of the directivity of a set of 4 distributed monopoles at $x = \pm 0.3$ m, $y = \pm 0.3$ m that radiate in phase measured in the horizontal plane at a distance of $r = 1$ m: actual directivity (left), 6th-order conventional representation (middle), and 6th-order proposed representation (right). The decompositions were obtained via an unregularized least-squares fit.

The frequency f' above which the roll-off occurs can be estimated roughly via [40]

$$f' = \frac{(L - L_\mathrm{s})\, c}{2\pi r_\mathrm{s}}\,, \tag{11}$$

whereby L_s is the order of the directivity of the source when centered at the coordinate origin (for the monopole, $L_\mathrm{s} = 0$), and r_s is the distance of the source position to the coordinate origin. This leads to $f' \approx 1100$ Hz for the scenarios depicted in Fig. 1 and 2. The proposed representation in Fig. 1(b) (right) and Fig. 2 (right) is capable of replicating the original magnitude directivity with much less deviation at any frequency. Potentially more importantly, the proposed representation does not exhibit a high-frequency roll-off because the sound source inherently appears in the coordinate center.

The concept of source centering was proposed in [9], [41], [40] to concentrate energy in the lower SH orders and avoid the high-frequency roll-off discussed above. It consists in identifying the acoustic centers of the elementary sound sources that the source comprises, whereby one is assumed for each frequency bin, and placing the coordinate origin in which the decomposition (3) is performed for the given frequency bin into the acoustic center. Note that this requires modifying the definitions of the matrices $\mathbf{Y}$ and $\mathring{\mathbf{W}}$ in (4) and (5) as detailed in [22].

We do not apply explicit source centering as our proposed representation (10) performs it inherently.

B. Other Considerations

Eq. (7) and consequently also the proposed representation (10) requires the source to be small compared to the observer distance r and the order L of the expansion to be sufficiently high. We demonstrated in [26] that these requirements are indeed fulfilled for the directivity of a reasonably compact loudspeaker that is well-centered in the microphone array during measurement. The resulting conventional and proposed directivity magnitudes can hardly be distinguished at order $L = 6$. We define the relative magnitude error (RME) as

$$E(\omega) = 20 \log_{10} \sum_{n=1}^{N} \frac{1}{N} \frac{\left| |\hat{W}_n(\omega)| - |W_n(\omega)| \right|}{|W_n(\omega)|}\,, \tag{12}$$

whereby n are the indices of the N measurement locations, $\hat{W}(\cdot)$ is either the conventional or the proposed directivity representation, and $W(\cdot)$ is the measured directivity. For both the conventional and for the proposed directivity representation of the loudspeaker from [26], which we will revisit in Sec. V-B, the RME is approx. -20 dB below 5 kHz and -10 dB above 5 kHz.

For sources that are not spatially compact or not located in the center of the microphone array with which their directivity is measured, the error of the conventional representation will actually be much larger than the error of the proposed representation. The RME of the conventional representation of the displaced monopole from Fig. 1 is lower than -100 dB below 1 kHz but approx. 0 dB above 1 kHz whereas the RME of the proposed representation is constant over the entire frequency range at approx. -200 dB.

The proposed approximation modifies the distance dependency of the directivity and makes the magnitude decay indirectly proportional to the distance r from the nominal source position as

$$|W'(r, \boldsymbol{\gamma}, \omega)| = \frac{|W(R, \boldsymbol{\gamma}, \omega)|}{r} R\,. \tag{13}$$

This alteration of the decay distance may be significant at short distances from a radiating surface that has a spatial extent that is considerable. The deviation of the decay distance vanishes at distances that are much larger than the largest dimension of

the source (where (7) holds) and solely a general amplitude offset may remain.

We evaluate (13) for the monopole from Fig. 1, which is located at $(x_\mathrm{s}, y_\mathrm{s}, z_\mathrm{s}) = (0.3, 0, 0)$ m and $R = 1$ m. All considerations apply to positions outside of the measurement sphere, i.e., $r \geq R$. The worst case occurs at $(x, y, z) = (R, 0, 0)$ where $|W'(r, \boldsymbol{\gamma}, \omega)|$ exhibits a magnitude error of 3.1 dB. The error drops to 1.4 dB at $(2R, 0, 0)$. The error is -2.3 dB at $(-R, 0, 0)$ and drops to -1.2 dB at $(2R, 0, 0)$. The error is never larger than -0.12 dB along the y and z axes.

The distance dependency of the proposed representation – as for any exterior sound field – is represented by the ratio of spherical Hankel functions $h_l^{(1)}(\cdot)$ in (10). Fig. 3 illustrates this ratio for a change in distance by a factor of 100. Besides the overall reduction of the amplitude, higher orders are attenuated progressively at low frequencies. The phase of the directivity is affected only at very low frequencies. For general exterior sound fields, the reduction of the amplitude of higher orders makes the wavefronts progressively more spherical (note that a spherical wave from the coordinate origin has 0th order). For the proposed directivity representation, it smooths the angular dependency. We did not find an effect on the overall spectral envelope for the proposed representation even for very far distances.

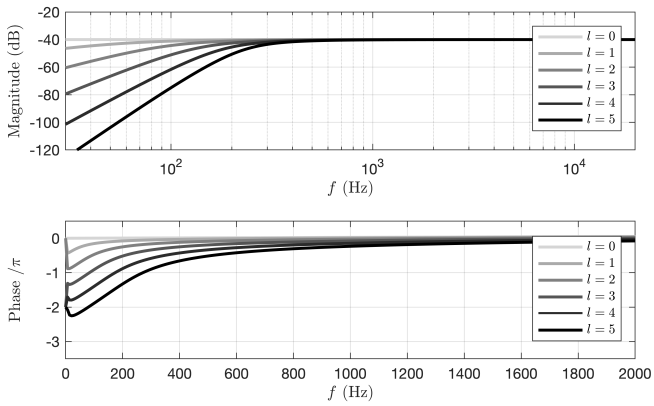

Fig. 3. Magnitude in dB (top) and unwrapped phase in multiples of π (bottom) of $h_l^{(1)}\left(100\frac{\omega R}{c}\right)/h_l^{(1)}\left(\frac{\omega R}{c}\right)$ for $R = 1$ m as a function of frequency for $0 \leq l \leq 5$. We removed the linear slope from the phase that represents the time delay for convenience. Note the different scalings of the frequency axis.

Other modifications that the proposed approximation applies to a directivity like changing the apparent position of source, its spatial extent, as well as the phase of the directivity are less tangible than the magnitude so that they need to be considered based on the particular application scenario.

Finally, all scenarios that we consider in this article assume that a sound source is small enough to fit within a spherical array of microphones. The size of the sources therefore has to be moderate for practical reasons. The radii of the corresponding arrays is in the order of 1.0 m–2.1 m [15], [21], [42]. There are indeed sound sources of interest such as trains, railway tracks, or machinery that do not fulfil this requirement. The deviation of the proposed representation from the actual directivity can indeed be considerable in such cases. It is likely to be less favorable to represent the radiation of such sources based on a spherical wave. Other wave front models such as that of a cylinder of finite length [43] seem more appropriate, and (9) and (10) need to be reformulated accordingly. Such scenarios are beyond the scope of this article.

V. Results

Geometric acoustics algorithms are able to incorporate SH-based sound source directivity data, even when incomplete (sparse and available over selected bands) [7], [6], [8], [3]. Wave-based methods such as, e.g., the finite difference time domain (FDTD) method [44], [45], [46], require more care in the incorporation of source directivity [47], [48], [49]. See, e.g., recent work allowing for the incorporation of measured directivity into an FDTD method, assuming a complete set of directivity data [12]. In this methodology, a measured directivity is used in order to construct a point-like multipole driving term in the model at the nominal source position which coincides with the origin of the coordinate system in (1). Such a point-like model is a natural fit to wave-based methods such as FDTD—see Appendix C for more details. We choose this most challenging application to validate our proposed directivity representation.

In all numerical examples presented in this section, the basic FDTD scheme given in (22) is used. The time step is chosen as $T = 1/44100$ s, and the scheme is run over a cubic region of side length 2 m, with second order Engquist Majda absorbing boundary conditions [50] on all faces.

Strictly speaking, (1) and (10) are so-called exterior representations that are only valid outside of a sphere that contains the sound source in its entire extent [29, p. 206]. By extrapolating the directivity to the center of the coordinate system, we actually penetrate the sound source whose directivity we are considering. This is particularly true when using the conventional representation (1). The actual virtual spatial extent of the source in the proposed representation (10) is not obvious. The consequence is that the directivity will not be meaningful when evaluated at such interior positions. However, (1) is a physically viable solution to the wave equation even in the interior domain so that we are not facing fundamental physical limitations here. The following subsection sheds some light on this aspect.

A. Numerical Conditioning

The numerical conditioning of the involved quantities deserves attention particularly in view of the fact that FDTD simulations extrapolate source directivities to positions inside the source and that source directivities have a singularity at the source position (the directivity of a point source (a 0th-order directivity) is $\propto 1/r$, and that of a dipole (a 1st-order directivity) is $\propto \omega^2/r^2$ [29, p. 198, 200]; cf. also [51, p. 40]).

We here investigate the numerical conditioning of the signals through which the sound source directivity is injected into the simulation framework. It is shown in [12] that a directivity that is available as a set of SH coefficients $\mathring{W}_{l,m}(R, \omega)$ (cf. (1)) over a sphere of finite radius R centered around the source can be directly substituted into an FDTD simulation

with appropriately defined SH driving functions $a_{l,m}(t)$—see Appendix C. Their Fourier transforms $\hat{a}_{l,m}(\omega)$ can be set as

$$\hat{a}_{l,m}(\omega) = \frac{4\pi c\ (-1)^l\ \mathrm{i}^l}{(\mathrm{i}\omega)^{l+1} h_l^{(1)}\left(\omega \frac{R}{c}\right)}\ \mathring{W}_{l,m}(R,\omega)\ . \qquad (14)$$

Each such signal $\hat{a}_{l,m}(\omega)$ determines the contribution of a single SH component, of indices l, m to the directivity.

Eq. (16) in Appendix B proves that (14) is numerically well-conditioned at high frequencies, and (17) proves that (14) is numerically well-conditioned at low frequencies. Note that we use (17) in this article to compute $\hat{a}_{l,m}(\omega)$ at very low frequencies.

B. Measured Directivity of a Loudspeaker

This section employs the measurement data on the IEM Loudspeaker Cube, a compact loudspeaker with a cube-shaped enclosure, provided in [52], [53]. The directivity is available as impulse responses measured on 648 equi-angularly spaced points with a spacing of 10° on a spherical surface of radius $R = 0.75$ m. They therefore allow for the computation of a complete ground-truth conventional representation of the directivity against which we can verify the proposed one.

The propagation delay from the loudspeakers to the measurement surface is not contained in the impulse responses. We therefore pre-padded a sufficient amount of silence to maintain causality of the ground truth data. The IEM Loudspeaker Cube comprises four identical drivers. We used the data of driver 1. As we demonstrated in [26], the deviation of the magnitude of the proposed representation from the conventional one is minuscule for the employed unregularized least-squares fit. We arbitrarily chose an order of $L = 6$. Either representation exhibits an RME (cf. Eq. (12)) between -20 dB and -10 dB for the vast part of the frequency range. Fig. 4 shows example data at two representative frequencies. No high-frequency roll-off is apparent due to the fact that the loudspeaker is compact and centered. The loudspeaker becomes very directional at high frequencies which is reflected by the very narrow lobe in the balloon plot in the bottom left plot. The chosen order limit of $L = 6$ in the SH representations is too low to reflect this, which results in slightly wider lobes (bottom center and bottom right), which means in turn that the directivity exhibits stronger high-frequency components in directions just off the main lobe. It also has to be taken into account that the data suffer from spatial aliasing, which occurs mainly above the frequency [54]

$$f_\mathrm{A} = \frac{L_\mathrm{grid} c}{2\pi R}\,, \qquad (15)$$

where L_grid is the maximum order that the angular sampling grid supports ($L_\mathrm{grid} = 15$ in the present case [51, Eq. (4.26)]). This leads to $f_\mathrm{A} \approx 1.2$ kHz. Spatial aliasing constitutes ambiguities in the spatial information and prevents extraction of the wave front curvature from the measurement data.

As an application example, Fig. 5 illustrates the time evolution of the acoustic field in an FDTD simulation using both the conventional and the proposed representations, whereby the latter employs a minimum phase $\phi(\gamma, \omega)$ in (8). A Gaussian pulse is used as input signal. The zone corresponding to the driving distribution is indicated by a white circle. The spherical curvature of the wave fronts of the proposed representation is evident in the right subplot in Fig. 5. We refer the reader to [26] for more simulations employing the same data.

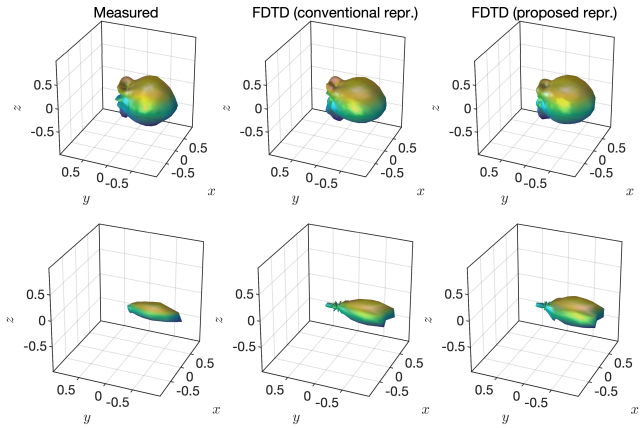

Fig. 4. Normalized balloon plots (in arbitrary units, a. u.) for the FDTD output of the data from Fig. 5 taken over a sphere of radius 0.75 m at a frequency of 818 Hz (top) and 5513 Hz (bottom). Left: measured directivity. Middle: 6th-order conventional representation. Right: 6th-order proposed representation.

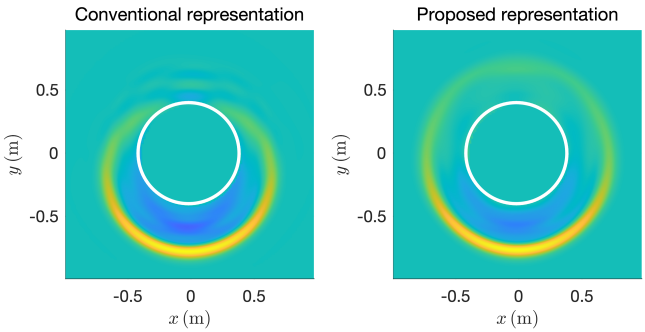

Fig. 5. Snapshot at $t = 3.6$ ms of a cross-section through the horizontal plane of the simulated acoustic field emitted by the IEM loudspeaker cube (cf. 4) using a Gaussian pulse of variance 1×10^{-4} as input signal. Here, we use the directivity data of driver 1, with the conventional representation (left) and the proposed one (right), both of 6th order.

C. Measured Directivity of a Musical Instrument

The measurement of the directivities of musical instruments is a significant challenge as the instruments cannot be driven with arbitrary dedicated measurement signals like sweeps. This section incorporates the data set of recordings of 41 different musical instruments made with an enclosing spherical array of 32 microphones and with radius $R = 2.1$ m that was presented in [21]. This leads to $f_\mathrm{A} \approx 100$ Hz (cf. Eq. (15)). Professional musicians played single notes as well as scales at two dynamic levels (pianissimo and fortissimo). It was proposed in [21] to identify the stable partial oscillations for each tone and define the observed magnitudes and phases at the corresponding frequencies as the directivity of the instrument at the according frequency of the oscillation. Fig. 6(a) depicts the signal recorded by microphone 1 of an oboe playing the note c5 ($f_0 = 523$ Hz), which is in the middle of the pitch range of an oboe, at fortissimo. Fig. 6(b) depicts the magnitude spectrum of the first segment that is marked by the blue horizontal bar in Fig. 6(a) with the stable partial oscillations marked.

We determined the magnitude and phase directivity according to above definition for all three segments marked in Fig. 6(a). The result is depicted in Fig. 7(a) and (b). It can be seen that the magnitudes are reasonably similar between the segments (cf. Fig. 7(a)) while the phases vary greatly (cf. Fig. 7(b)). This shows that the articulation has significant influence on the measured phase of the directivity even within such a short segment that was being played as stationary as the player was able to do it. Note that we did not apply interpolation of the spectral peaks when determining the frequency, magnitude, and phase. This was because the peaks did not appear to be so clean that a simple curve like the quadratic one used in [55] could be fitted onto the bins surrounding a peak.

We found comparable results in the data from [21] for instruments including the acoustic guitar where the sustain and decay of the tones are autonomous and are not affected by the player.

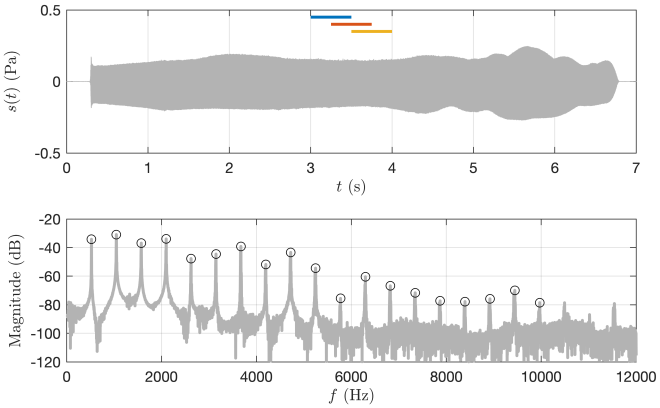

Fig. 6. Signal recorded by microphone 1 for the oboe playing c5 ($f_0 = 523$ Hz) at fortissimo. Top: time domain signal with 3 segments marked by the horizontal bars. Bottom: magnitude spectrum of segment 1 with all stable harmonics below 10 kHz marked

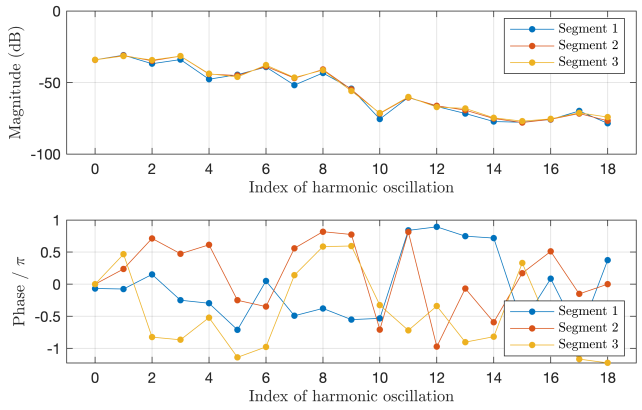

Fig. 7. Magnitude (top) and phase relative to the fundamental oscillation (bottom) of the directivity of the oboe playing the note c5 ($f_0 = 523$ Hz) at fortissimo derived based on the 3 segments marked in Fig. 6. The data points are connected with straight lines for legibility.

Another important observation that was made in [9], [15] is that the magnitude and phase of the directivity change substantially with the played note and dynamic level. Fig. 8 depicts the magnitudes of the harmonic oscillations of the oboe relative to the direction straight ahead for three notes at third-octave intervals at fortissimo level. Differences of up to 10 dB are apparent.

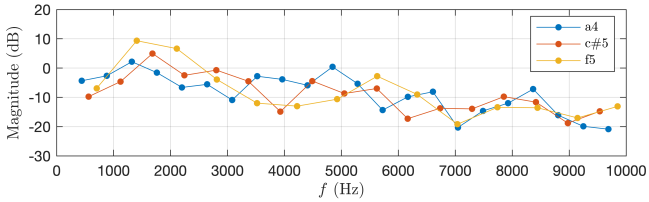

Fig. 8. Magnitudes of the harmonic oscillations of the oboe in direction $(\alpha, \beta) = (144°, 101°)$ for three notes normalized to the direction straight ahead. The corresponding fundamental frequencies are 440 Hz, 554 Hz, and 659 Hz. The data points of each note are connected with straight lines for legibility.

Fig. 9 depicts the directivity of the oboe for one specific played note over the entire frequency range of interest. The data were obtained via linear interpolation of the magnitudes of the measured directivity at the frequencies where measurement data were available (blue line), separate interpolation of the magnitude and of the phase[2] of the measured directivity together with an unregularized fit of a conventional representation according to (1) (orange line), and the proposed representation according to (10) (yellow line). The interpolation of the measured magnitudes is required for being able to evaluate the different representations in directions between the measurement points. The proposed representation was computed by complementing the interpolated magnitudes of the measured directivity with a minimum phase factor $\phi(\boldsymbol{\gamma}, \omega)$ in (8) and an unregularized SH fit. The SH representations are of 4th order.

Note that no high-frequency roll-off like in Fig. 1(b) is apparent even with the conventional representation in Fig. 9. A possible explanation may be ambiguities in the measured phases that obscure the actual wave front. Spatial aliasing is apparent above $f_\mathrm{A} \approx 100$ Hz (Eq. (15)), and the phases were extracted from a steady-state deterministic signal so that the actual propagation time of the sound wave from the source to the array cannot be deduced, only the relative phase between the harmonic oscillations.

Pronounced deviations of the magnitude transfer function of the conventional representation from interpolated measured magnitudes occur. This is primarily a consequence of the difficulties when interpolating complex data with respect to frequency [26]. The conventional representation tends to be close to the measured directivity at frequencies at which the data were measured, i.e. where no interpolation was performed (cf. Fig. 10, top row). The RME is comparable for both conventional and proposed representation and around -20 dB at these frequencies. The large deviations of the conventional representation tend to occur at frequencies between measurement points (cf. Fig. 10, bottom row), where no RME can be computed as no ground truth is available.

[2]Note that it is currently unclear if interpolation of the complex data or of magnitude and phase separately is more favorable. Similar observations were made in the interpolation of head-related transfer functions were some authors use interpolation of the complex data whereas other authors use interpolation of the magnitude and phase [30], [56].

The notches in the magnitude spectrum of the conventional directivity representation that are apparent in Fig. 9 are accompanied by a smearing of the information in time domain. This is reflected in the impulse-response representation of the directivity in Fig. 11 and the time-domain FDTD snapshots in Fig. 12. The proposed representation has a shorter support over time. Differences in the overall magnitude are also apparent, for example, along the positive x-axis. Finally, the curvature of the wavefronts of the conventional representation is not plausible. The oboe player was located in the center of the spherical microphone array and facing into positive x-direction which suggests that the instrument itself was displaced in direction of the positive x-direction. The observed curvature suggests that the source was displaced towards the negative x axis by approx. 0.16 m. Possible causes for this implausibility are spatial aliasing and other ambiguities of the phase data due to the measurement setup (recall Fig. 7).

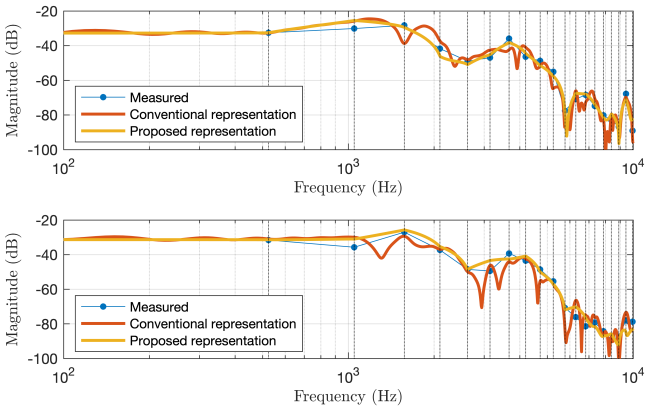

Fig. 9. Magnitude of the directivity of the oboe playing c5 ($f_0 = 523$ Hz) at fortissimo in two arbitrarily chosen sample directions $(\alpha, \beta) = (108°, 37°)$ (top) and $(36°, 79°)$ (bottom). The vertical black dotted lines mark the frequencies of the partial oscillations. The SH representations are of 4th order.

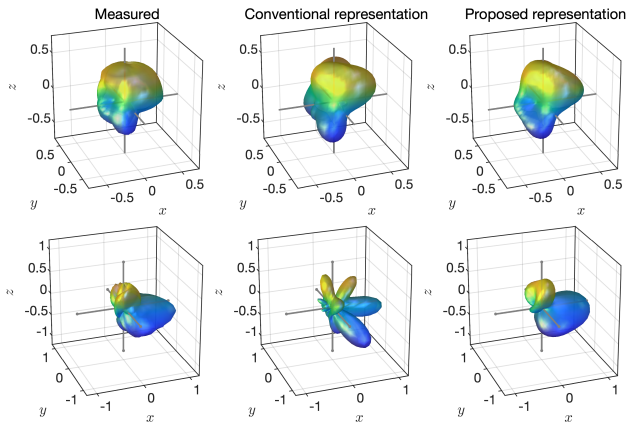

Fig. 10. Balloon plots of the directivity of the oboe playing c5 ($f_0 = 523$ Hz) at fortissimo. Top: The depicted frequency coincides with the fundamental oscillation of the played note. Bottom: The depicted frequency of $f = 1873$ Hz is between two harmonic oscillations. In this case, the 'measured' data were computed from interpolating the available magnitude data points over frequency and then over the measurement sphere using a cylindrical projection.

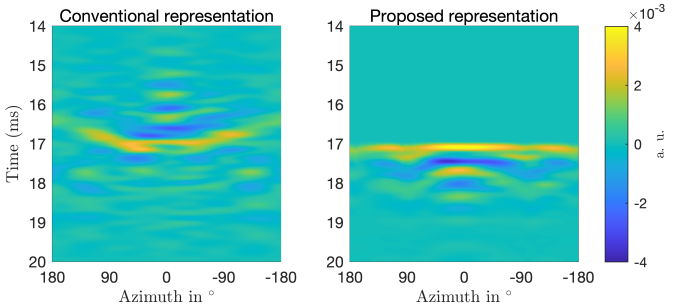

Fig. 11. Impulse response representation of the data from Fig. 9 and 10 in the horizontal plane

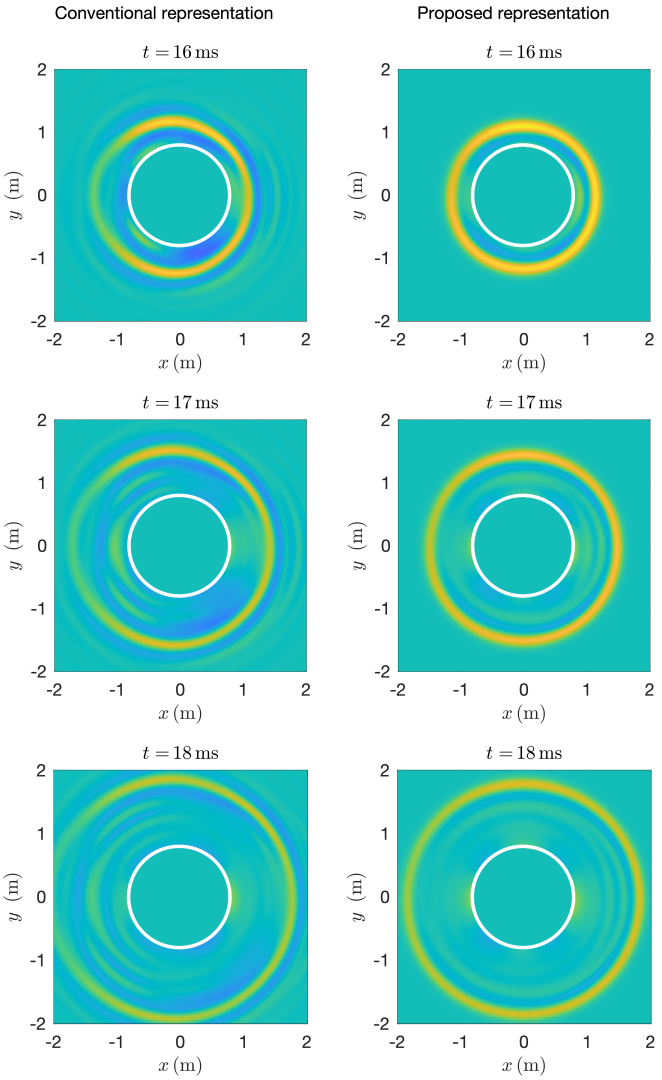

Fig. 12. Snapshots of a cross-section of the simulated acoustic field emitted by source with directivity like an oboe playing the note c5, ff, 4th order, using a Gaussian pulse of variance 1×10^{-4} as input signal. Conventional representation (left) (center column in Fig. 10) and proposed representation (right) (right column in Fig. 10), both of 4th order. The timing was aligned such that the strongest parts of the signals occur at the same time.

VI. Conclusions

We have explored a spherical harmonic (SH) representation for sound source directivity that is based on the design of a directivity such that its magnitude matches the finite-distance magnitude signature of the measured directivity on a spherical

surface around the sound source. The approach is required to mitigate the challenges that arise from the use of incomplete or unreliable measurement data, which can usually not be avoided when considering non-electroacoustic sources. The limitations of the measurement data may be the following:

- The directivity data are only available at a sparse set of frequencies.
- Only the frequency-dependent magnitude of the directivity data may be available. With musical instruments, the phase is strongly dependent on the time instant of a steady note that is being played. It is unclear how to determine what data are representative. This circumstance seems to be more pronounced with some instruments than with others. A detailed analysis of the aspect is beyond the scope of this article. Directivity data of machinery and the like will most likely not contain phase data at all.
- Even if the phase is available, interpolation of complex spectral data over frequency does not produce favorable results as undesired notches can occur.

Additionally, the proposed representation does not suffer from the high-frequency roll-off that classical spherical harmonic representations of displaced sound sources exhibit. The viability of the resulting representations needs to be evaluated in an application-specific manner in the future as no general ground truth is available against which the results can be compared. This will help evaluating the effect of some of the modifications that the proposed representation applies to a directivity that are less tangible such as changing the apparent position of the source, its spatial extent, and its phase.

All SH representations from this article are available at [57].

APPENDIX A
CONVERGENCE OF THE SIGNALS $\hat{a}_{l,m}(\omega)$

We study the convergence of (14) with respect to frequency in the following. Applying the large-argument approximation of the spherical Hankel function given by (18) to (14) yields

$$\hat{a}_{l,m}(\omega) = \frac{4\pi R}{(\mathrm{i}\omega)^l} \mathrm{e}^{-\mathrm{i}\omega\frac{R}{c}} \mathring{W}_{l,m}(R,\omega), \quad \text{as} \quad \omega \to \infty \,, \tag{16}$$

which converges for high frequencies (assuming that the coefficients $\mathring{W}_{l,m}(R,\omega)$ converge).

Applying the small-argument approximation of the spherical Hankel function given by (19) to (14) yields

$$\hat{a}_{l,m}(\omega) = \frac{4\pi c\,(-1)^l}{(2l-1)!!} \left(\frac{R}{c}\right)^{l+1} \mathring{W}_{l,m}(R,\omega), \quad \text{as} \quad \omega \to 0 \,, \tag{17}$$

which converges for low frequencies.

APPENDIX B
APPROXIMATIONS OF SPHERICAL HANKEL FUNCTIONS

The large argument approximation of the spherical Hankel function is given by [29, p. 197]

$$h_l^{(1)}(x) \approx (-\mathrm{i})^{l+1} \frac{\mathrm{e}^{\mathrm{i}x}}{x} \quad \text{as} \quad x \to \infty \,. \tag{18}$$

The small argument approximation of the spherical Hankel function is given by [29, p. 197]

$$h_l^{(1)}(x) \approx -\mathrm{i} \frac{(2l-1)!!}{x^{l+1}} \quad \text{as} \quad x \to 0 \,. \tag{19}$$

APPENDIX C
SOURCE MODELING IN FDTD

Source modeling in time domain wave-based virtual acoustics has been covered by various authors using a variety of techniques, as mentioned in Section V. The approach here, following [12] is to model the source as an additional driving term in the wave equation:

$$\frac{1}{c^2}\partial_t^2 p - \Delta p = \sum_{l=0}^{\infty} \sum_{m=-l}^{l} c^l \left(g * a_{l,m}\right)(t) D_{l,m} \delta^{(3)}(\mathbf{r}) \,. \tag{20}$$

Here, $p(\mathbf{r},t)$ is the acoustic pressure, as a function of time t and spatial coordinate $\mathbf{r} \in \mathbb{R}^3$. c is the wave speed, ∂_t represents partial differentiation with respect to time, and Δ is the 3D Laplacian. The wave equation is driven by a series of terms, each of which activates a single spherical harmonic directivity pattern. Each term includes a point source at the coordinate origin modelled by a 3D Dirac delta function $\delta^{(3)}(\mathbf{r})$ under the action of a differential operator $D_{l,m}$ defined by

$$D_{l,m} = Y_{l,m}(\nabla) \tag{21}$$

in terms of the 3D gradient ∇. The system is assumed driven by a scalar source signal $g(t)$, with the (l,m)th channel filtered by the functions $a_{l,m}(t)$ given by (14) in order determine the directivity of the source. See [12].

In the case of FDTD, the numerical solution $p_{\mathbf{q}}^n$, for integer n and $\mathbf{q} \in \mathbb{Z}^3$ represents an approximation to $p(\mathbf{r},t)$ at $t = nT$ and $\mathbf{r} = \mathbf{q}X$, where T is the time step, and X is the grid spacing. Using a very basic seven-point approximation to the Laplacian, the following scheme results:

$$\begin{aligned} p_{\mathbf{q}}^{n+1} \quad = \quad & 2p_{\mathbf{q}}^n - p_{\mathbf{q}}^{n-1} + \lambda^2 \sum_{\mathbf{e}\in\mathbb{Q}} \left(p_{\mathbf{q}+\mathbf{e}}^n - p_{\mathbf{q}}^n\right) \\ & + T^2 \sum_{l=0}^{\infty} \sum_{m=-l}^{l} c^{l+2} \left(g * a_{l,m}\right)^n d_{l,m} s_{\mathbf{q}} \,, \end{aligned} \tag{22}$$

Here, $\lambda = cT/X \leq 1/\sqrt{3}$ is the scheme Courant number, and $\mathbb{Q}$ is the set of 3-vectors of unit L_1 norm, defining the seven-point stencil. g^n and $a_{l,m}^n$ are discrete time signals derived from $g(t)$ and $a_{l,m}(t)$ respectively, and $s_{\mathbf{q}}$ is an approximation to the 3D Dirac delta function (in the simplest case, a Kronecker delta at $\mathbf{q} = \mathbf{0}$ scaled by $1/X^3$. $d_{l,m}$ is a difference approximation to the differential operator $D_{l,m}$.

REFERENCES

[1] J. Meyer, *Acoustics and the Performance of Music*. New York: Springer, 2009.

[2] F. Otondo and J. H. Rindel, "The influence of the directivity of musical instruments in a room," *Acta Acustica utd. w. Acustica*, vol. 90, pp. 1178–1184, 2004.

[3] J. Klein and M. Vorländer, "Simulative investigation of required spatial source resolution in directional room impulse response measurements," in *Proc. of EAA Spatial Audio Sig. Proc. Symp*, 2019, pp. 37–42.

[4] R. Janczur, E. Walerian, M. Meissner, and M. Czechowicz, "Influence of vehicle noise emission directivity on sound level distribution in a canyon street. Part II: experimental verification," *Applied Acoustics*, vol. 67, no. 7, pp. 659–679, 2006.

[5] R. Mehra, L. Antani, S. Kim, and D. Manocha, "Source and listener directivity for interactive wave-based sound propagation," *IEEE Trans. Visualization Comp. Graphics*, vol. 20, no. 4, pp. 83–94, 2014.

[6] B. Postma, H. Demontis, and B. Katz, "Subjective evaluation of dynamic voice directivity for auralizations," *Acta Acustica united with Acustica*, vol. 103, no. 2, pp. 181–184, 2017.

[7] J. H. Rindel, F. Otondo, and C. L. Christensen, "Sound source representation for auralization," in *Proc. of Int. Symp. on Room Acoustics*, Hyogo, Japan, 2004, pp. 1–8.

[8] G. Götz and V. Pulkki, "Simplified source directivity rendering in acoustic virtual reality using the directivity sample combination," in *147th Convention of the AES*, New York, NY, USA, Oct. 2019, p. 10286.

[9] F. Zotter, "Analysis and synthesis of sound-radiation with spherical arrays," Ph.D. dissertation, University of Music and Dramatic Arts, Graz, 2009.

[10] M. Pollow, "Directivity patterns for room acoustical measurements and simulations," PhD thesis, RWTH Aachen, 2014.

[11] G. Weinreich and E. B. Arnold, "Method for measuring acoustic radiation fields," *J. Acoust. Soc. Am.*, vol. 68, no. 2, pp. 404–411, 1980.

[12] S. Bilbao, J. Ahrens, and B. Hamilton, "Incorporating source directivity in wave-based virtual acoustics: Time-domain models and fitting to measured data," *J. Acoust. Soc. Am.*, no. (in press), 2019.

[13] M. Frank and M. Brandner, "Perceptual evaluation of spatial resolution in directivity patterns," in *Proc. of DAGA*, Rostock, Germany, 2019, pp. 1–4.

[14] D. Cabrera, P. J. Davis, and A. Connolly, "Long-term horizontal vocal directivity of opera singers: Effects of singing projection and acoustic Environment," *Journal of Voice*, vol. 25, no. 6, pp. e291–e303, 2011. [Online]. Available: http://dx.doi.org/10.1016/j.jvoice.2010.03.001

[15] J. Pätynen and T. Lokki, "Directivities of symphony orchestra instruments," *Acta Acustica Utd. with Acustica*, vol. 96, no. 1, pp. 138–167, 2010.

[16] P. Mioduszewski and J. A. Ejsmont, "Directivity of tire/road noise emission for selected tires and pavements," *Noise Control Engineering Journal*, vol. 57, no. 2, pp. 129–138, 2009.

[17] D. Thompson, *Railway Noise and Vibration*. New York: Elsevier Science, 2010.

[18] S. Oerlemans and J. G. Schepers, "Prediction of wind turbine noise and validation against experiment," *Aeroacoustics*, vol. 8, no. 6, pp. 555–584, 2009.

[19] CLF Group, "Common loudspeaker format," Available online at http://www.clfgroup.org/ (Last viewed 06/05/2019), 2019.

[20] L. M. Wang and C. B. Burroughs, "Acoustic radiation from bowed violins," *The Journal of the Acoustical Society of America*, vol. 110, no. 1, pp. 543–555, 2001. [Online]. Available: https://doi.org/10.1121/1.1378307

[21] N. Shabtai, G. Behler, M. Vorländer, and S. Weinzierl, "Generation and analysis of an acoustic radiation pattern database for forty-one musical instruments," *J. Acoust. Soc. Am.*, vol. 141, no. 2, pp. 1246–1256, 2017.

[22] N. Shabtai and M. Vorländer, "Acoustic centering of sources with high-order radiation patterns," *J. Acoust. Soc. Am.*, vol. 137, no. 4, pp. 1947–1961, 2015.

[23] C. Anemüller and J. Herre, "Calculation of directivity patterns from spherical microphone array recordings," in *147th Convention of the AES*, New York, NY, USA, Oct. 2019, p. 10285.

[24] J. Ahrens and S. Bilbao, "Interpolation and range extrapolation of sound source directivity based on a spherical wave propagation model," in *IEEE ICASSP*, Barcelona, Spain, May 2020.

[25] J. Ahrens and S. Spors, "Wave field synthesis of moving virtual sound sources with complex radiation properties," *J. Acoust. Soc. Am.*, vol. 130, no. 5, pp. 2807–2816, 2011.

[26] J. Ahrens and S. Bilbao, "Computation of spherical harmonics based sound source directivity models from sparse measurement data," in *Forum Acusticum*, Lyon, France, May 2020.

[27] J. Meyer, *Acoustics and the Performance of Music*. New York: Springer, 2009.

[28] D. Blackstock, *Fundamentals of Physical Acoustics*. New York, NY: Wiley-Interscience, 2000.

[29] E. Williams, *Fourier Acoustics: Sound Radiation and Nearfield Acoustical Holography*. New York: Academic Press, 1999.

[30] D. N. Zotkin, R. Duraiswami, and N. Gumerov, "Regularized HRTF fitting using spherical harmonics," in *IEEE WASPAA*, New Paltz, NY, USA, Oct. 2009, pp. 257–260.

[31] J. Ahrens, M. R. P. Thomas, and I. Tashev, "HRTF magnitude modeling using a non-regularized least-squares fit of spherical harmonics coefficients on incomplete data," in *Proc. of APSIPA*, Hollywood, CA, USA, December 2012, pp. 1–5.

[32] S. Boyd and L. Vandenberghe, *Convex Optimization*. Cambridge, UK: Cambridge University Press, 2004.

[33] N. Gumerov and R. Duraiswami, *Fast Multipole Methods for the Helmholtz Equation in Three Dimensions*. Amsterdam: Elsevier, 2005.

[34] B. Girod, R. Rabenstein, and A. Stenger, *Signals and Systems*. New York: J.Wiley & Sons, 2001.

[35] F. Zagala and F. Zotter, "Idea for sign-change retrieval in magnitude directivity patterns," in *Proc. of DAGA*, Rostock, Germany, 2019, pp. 1–4.

[36] P. W. Kassakian, "Convex Approximation and Optimization with Applications in Magnitude Filter Design and Radiation Pattern Synthesis," Ph.D. dissertation, University of California Berkeley, 2006.

[37] A. Canclini, F. Antonacci, S. Tubaro, and A. Sarti, "A methodology for the robust estimation of the radiation pattern of acoustic sources," *IEEE/ACM TASLP*, vol. 28, pp. 211–224, 2019.

[38] R. Baumgartner, "Time domain fast-multipole translation for ambisonics," Diplom Thesis, University for Music and Dramatic Arts, Graz, 2011.

[39] N. Hahn and S. Spors, "Physical properties of modal beamforming in the context of data-based sound reproduction," in *139th Convention of the AES*, New York, NY, USA, Oct. 2015, p. 9468.

[40] I. B. Hagai, M. Pollow, M. Vorländer, and B. Rafaely, "Acoustic centering of sources measured by surrounding spherical microphone arrays," *J. Acoust. Soc. Am.*, vol. 130, no. 4, pp. 2003–2015, 2011.

[41] D. Deboy and F. Zotter, "Acoustic center and orientation analysis of sound-radiation recorded with a surrounding spherical microphone array," in *Proc. of the 2nd Int. Symposium on Ambisonics and Spherical Acoustics*, Paris, France, 2010.

[42] M. Brandner, M. Frank, and D. Rudrich, "DirPat—Database and Viewer of 2D/3D Directivity Patterns of Sound Sources and Receivers," in *144th Convention of the AES*, Milan, Italy, May 2018, p. eBrief:425.

[43] Z. Ye, "A novel approach to sound scattering by cylinders of finite length," *J. Acoust. Soc. Am.*, vol. 102, no. 2, pp. 877–884, 1997.

[44] O. Chiba, T. Kashiwa, H. Shimoda, S. Kagami, and I. Fukai, "Analysis of sound fields in three dimensional space by the time-dependent finite-difference method based on the leap frog algorithm," *J. Acoust. Soc. Japan*, vol. 49, pp. 551–562, 1993.

[45] D. Botteldooren, "Acoustical finite-difference time-domain simulation in a quasi-cartesian grid," *J. Acoust. Soc. Am.*, vol. 95, no. 5, pp. 2313–2319, 1994.

[46] L. Savioja, T. Rinne, and T. Takala, "Simulation of room acoustics with a 3-D finite-difference mesh," in *Proc. of ICMC*, Århus, Denmark, sep 1994, pp. 463–466.

[47] J. Escolano, J. Lopez, and B. Pueo, "Directive sources in acoustic discrete-time domain simulations based on directivity diagrams," *JASA Express Lett.*, vol. 121, pp. 256–262, 2007.

[48] A. Southern and D. Murphy, "Low complexity directional sound sources for finite difference time domain room acoustic models," in *Proc. 126th Audio Eng. Soc. Conv.*, Munich, Germany, 2009.

[49] D. Takeuchi, K. Yatabe, and Y. Oikawa, "Source directivity approximation for finite-difference time-domain simulation by estimating initial value," *J. Acoust. Soc. Am.*, vol. 145, no. 4, pp. 2638–2649, April 2019.

[50] B. Engquist and A. Majda, "Absorbing boundary conditions for the numerical evaluation of waves," *Math. Comp.*, vol. 31, no. 139, pp. 629–651, 1997.

[51] J. Ahrens, *Analytic Methods of Sound Field Synthesis*. Heidelberg, Germany: Springer, 2012.

[52] N. Meyer-Kahlen, F. Zotter, and K. Pollack, "Design and measurement of first-order, horizontally beam-controlling loudspeaker cube," in *144th Convention of the AES, e-Brief 447*, Milan, Italy, May 2018.

[53] F. Zotter, "High-resolution directional impulse responses of the iem loudspeaker cubes," Available online at https://phaidra.kug.ac.at/detail/o:70240 (Last viewed 06/05/2019), 2019.

[54] B. Rafaely, "Analysis and design of spherical microphone arrays," *IEEE Trans. on Speech and Audio Proc.*, vol. 13, no. 1, pp. 135–143, 2005.

[55] J. Smith and X. Serra, "PARSHL: An analysis/synthesis program for non-harmonic sounds based on a sinusoidal representation," in *Proc. of the Int. Computer Music Conf. (ICMC)*, Champaign/Urbana, Illinois, USA, Aug. 1987.

[56] M. J. Evans, J. A. S. Angus, and A. I. Tew, "Analysing head-related transfer function measurements using surface spherical harmonics," *J. Acoust. Soc. Amer.*, vol. 104, no. 4, pp. 2400–2411, 1998.

[57] J. Ahrens, "Database of spherical harmonic representations of sound source directivities," Zenodo, DOI: 10.5281/zenodo.3707708, available online also at https://github.com/AppliedAcousticsChalmers/sound-source-directivities/, 2020.